Flowering in bursting bubbles with viscoelastic interfaces

Daniele Tammaro[a], Vinny Chandran Suja[b,1], Aadithya Kannan[b,1], Luigi Davide Gala[a], Ernesto Di Maio[a], Gerald G. Fuller[b], and Pier Luca Maffettone[a,2]

[a]Dipartimento di Ingegneria Chimica, Materiali e della Produzione Industriale, University of Naples Federico II, I-80125 Napoli, Italy; and [b]Department of Chemical Engineering, Stanford University, Stanford, CA 94305

Edited by Jens Eggers, University of Bristol, Bristol, United Kingdom, and accepted by Editorial Board Member Pablo G. Debenedetti June 23, 2021 (received for review March 17, 2021)

The lifetime of bubbles, from formation to rupture, attracts attention because bubbles are often present in natural and industrial processes, and their geometry, drainage, coarsening, and rupture strongly affect those operations. Bubble rupture happens rapidly, and it may generate a cascade of small droplets or bubbles. Once a hole is nucleated within a bubble, it opens up with a variety of shapes and velocities depending on the liquid properties. A range of bubble rupture modes are reported in literature in which the reduction of a surface energy drives the rupture against inertial and viscous forces. The role of surface viscoelasticity of the liquid film in this colorful scenario is, however, still unknown. We found that the presence of interfacial viscoelasticity has a profound effect in the bubble bursting dynamics. Indeed, we observed different bubble bursting mechanisms upon the transition from viscous-controlled to surface viscoelasticity-controlled rupture. When this transition occurs, a bursting bubble resembling the blooming of a flower is observed. A simple modeling argument is proposed, leading to the prediction of the characteristic length scales and the number and shape of the bubble flower petals, thus paving the way for the control of liquid formulations with surface viscoelasticity as a key ingredient. These findings can have important implications in the study of bubble dynamics, with consequences for the numerous processes involving bubble rupture. Bubble flowering can indeed impact phenomena such as the spreading of nutrients in nature or the life of cells in bioreactors.

bubble | surface | protein | flowering

When residing in Newtonian fluids, bubble rupture proceeds with features that are shown in Fig. 1. Different dynamics are observed depending on the capillary number, $Ca = u \quad \eta/\gamma$, where u is the experimentally measured characteristic retraction speed of the film, η is the liquid viscosity, and γ is the surface tension between the liquid and gas, and the Reynolds number, $Re = \rho u R_{\text{bubble}}/\eta$, where ρ is the liquid density, and R_{bubble} is the bubble radius (1–7). Fig. 1 *A*–*D* report observed bubble ruptures in the different regimes previously discussed in the literature: 1) for $Re \ll 1$, viscous forces are larger than inertial and surface forces, resulting in a very slow hole opening (8) (Fig. 1*A*); 2) when $Re > 1$, the hole opens up much more quickly (9), and a toroidal rim (Fig. 1*B*) is subjected to an azimuthal instability, which leads to fingering and, possibly, jetting (Fig. 1 *B*–*D*), depending on the corresponding Ca value. If $Ca \gg 1$, the rim is stable and folds upward (10); otherwise, inertial instabilities break it into pieces with a characteristic length scale, $d = \sqrt{R_{\text{bubble}} h}$, where h is the film thickness (11).

Here, we report evidence of the effect of surface viscoelasticity in bubble rupture dynamics. Surface viscoelasticity is adjusted by adding a surface-active material to the bulk and modulating its concentration and chemistry. We chose bovine serum albumin (BSA) proteins (12, 13), as they are known to form highly viscoelastic surface layers. At low concentrations, BSA molecules are adsorbed at the air/water interface with their major axis parallel to the surface. No protein denaturation occurs, and the molecules retain their globular conformation. As the concentration of BSA increases, a primary monolayer achieves full surface coverage, and a secondary monolayer appears, extending into the aqueous phase (14, 15). Adsorbed protein molecules are connected by interprotein contacts forming an interconnected network within the adsorbed layers (16). Upon compression, globular proteins, such as BSA, respond as deformable spheres, thereby being capable of storing elastic energy (yielding high storage moduli) (17). Many examples can be found in the literature in which the addition of surfactants to the protein solution can drastically change surface properties, giving an unlimited variety of model systems to achieve desired surface properties with a straightforward tuning of the surfactant concentration (18).

Results and Discussion

Surface elasticity introduces another dimensionless parameter, the elastocapillary number (19), $E_c = \frac{E_d}{\gamma}$, where E_d is the surface initial dilatation modulus measured for each concentration (*SI Appendix*). We carried out an extensive array of experiments to analyze the effects of E_c on the bubble rupture dynamics.

We report that surface viscoelasticity drives bubble rupture during opening, and the rupture shape changes as the concentration of BSA

Significance

The bursting bubbles are central in many natural and engineering processes because they influence the heat, mass, and momentum transfer; for example, fragmentation and cell death are influenced by the mechanical stresses produced by the hydrodynamic flows caused by the fast and frequent bubble bursting on viscoelastic surfaces in bioreactors. We investigate the bursting bubbles with viscoelastic interfaces and demonstrate that the interfacial viscoelasticity changes the bubble rupture mode. We present the characteristics of the bubble rupture mode that produces flower-shape bubble bursting and a validated modeling that can predict the number of petals formed during the rupture. This work presents insights for understanding and controlling the bursting bubbles with viscoelastic interfaces with both fundamental and practical implications.

Author contributions: D.T., A.K., E.D.M., G.G.F., and P.L.M. proposed the research; D.T., V.C.S., A.K., and L.D.G. performed the experiments and the fluids characterization; D.T., V.C.S., L.D.G., and E.D.M. analyzed the data; D.T., G.G.F., and P.L.M. performed the modelling; and D.T., E.D.M., G.G.F., and P.L.M. wrote the manuscript.

The authors declare no competing interest.

This article is a PNAS Direct Submission. J.E. is a guest editor invited by the Editorial Board.

[1]V.C.S. and A.K. contributed equally to this work.

[2]To whom correspondence may be addressed. Email: p.maffettone@unina.it.

This article contains supporting information online at https://www.pnas.org/lookup/suppl/doi:10.1073/pnas.2105058118/-/DCSupplemental.

Published July 22, 2021.

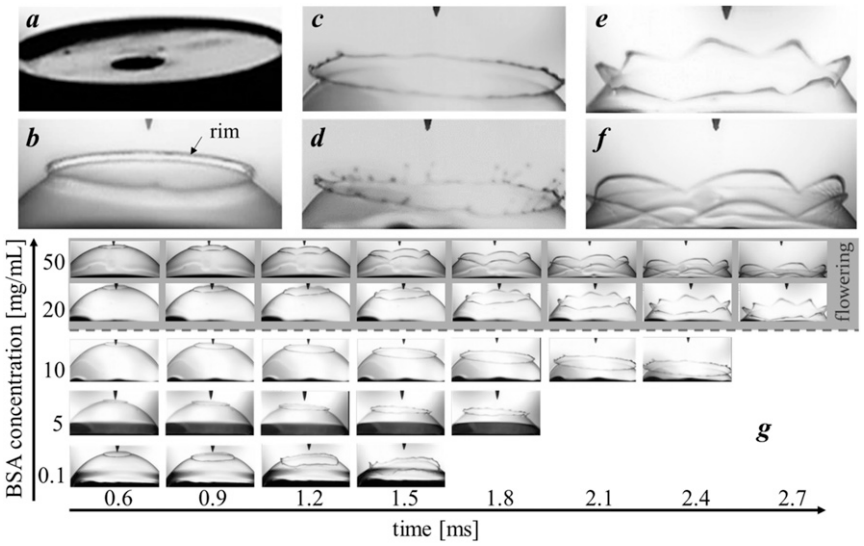

Fig. 1. Bubble bursting dynamics. (*A*) Low *Re*. (*B* and *C*) High *Ca* and high *Re*. (*D*) Low *Ca* and high *Re*. (*E*) Low *Ca* and high *Re* with intermediate interfacial viscoelasticity (20 mg/mL of BSA). (*F*) Low *Ca* and high *Re* with high interfacial viscoelasticity (50 mg/mL of BSA). (*G*) Bubble rupture as functions of time for different concentrations of BSA. Increasing the concentration of BSA leads to an increase in the surface viscoelasticity, and the bubble bursting dynamics change. The concentration of 20 mg/mL is identified as the limit above which flowering occurs. The number of petals, 10 at 20 mg/mL, decreases to 5 when the concentration of BSA is increased to 50 mg/mL. The bursting time (from the puncture to complete film retraction) increases when BSA is added, and it changes from 1.5 ms at 0.1 mg/mL to 2.7 ms at 50 mg/mL.

increases (Fig. 1 *E* and *F*) (Movie S1). In later stages of bubble rupture at a high BSA concentration in Fig. 1*G* (20 mg/mL shown in Movie S2, 50 mg/mL shown in Movie S3, and 15 mg/mL shown in Movie S4), we observe that the rim fractures during opening, thus forming liquid petals similar to a flower blooming.

The complete picture observed in the experiments at large BSA concentrations is shown in Fig. 2*B*: the initial stage of hole opening (with the radius equal to R_0) sees the formation of a toroidal rim (with the radius equal to R_i) that progressively grows in diameter followed by a developing rim breaking into small pieces (when the radius reaches R_b). The final stage has cracks growing radially through the bubble film with a velocity higher than the rim retraction speed producing triangular- or trapezoidal-shaped strips. The combined effects of inertia and capillarity lead to an outward trajectory of the strips and formation of a flower-shape rupture. A schematic of the experimental observation is reported in Fig. 2*A*.

We quantitatively illustrate the opening dynamics by following the hole perimeter rather than its radius since the perimeter (P) also accounts for the borders created by the cracks. At the lowest concentration in which interfacial viscoelasticity is less important, the trend shown in Fig. 2*C* is very similar to that found by Petit et al. and McEntee et al. (10, 20) for bubbles lacking viscoelasticity with an initial long linear increase of the rim perimeter, corresponding to a constant opening velocity. The behavior is similar to the inertial regime predicted by Culick and Taylor (9) but with a slower velocity, and Petit et al. (20) ascribe such a slowing down to the surface properties in the presence of surfactants. We reported the retraction speed of the rim, u, before the rim crack, as a function of the BSA concentrations in Fig. 3*C*, where u_c is the Taylor–Culick velocity, $u_c = \sqrt{\frac{\phi}{\rho}\frac{\gamma}{h}}$, [$\gamma$ is the surface tension, and ϕ is a constant ca. 2 depending on the film thickness (10)]. The decrease of velocity is ca. 20% at the highest concentration of BSA, and it affects *Re* ($\sim 10^3$) and *Ca* ~ 1); however, no different bursting dynamics are expected from the literature (3). However, at larger surface concentrations (20, 35, and 50 mg/mL), the rim opening follows three sequential regimes: an initial regime with the rim opening following a constant velocity similar to that at lower concentrations, a faster intermediate regime that commences following rim cracking ($t = t_{\mathrm{crack}}$) and petal blooming, and a final regime, which is initiated when crack propagation stops corresponding to a slowdown of the rim opening. In a dimensionless form, the data (Fig. 2*C*) for the three different BSA concentrations superimpose in the initial regime, thus confirming the time scaling $\left(t^* = \frac{t}{\frac{\rho h}{\gamma}}\right)$. Also notice that in the intermediate faster regime, the cracks propagate within the viscoelastic membrane at a velocity comparable with the sound velocity (refer to the data in *SI Appendix*) as found by Huang et al. (21). The cracks propagate into the membrane, releasing elastic energy stored during the bubble inflation process and stop once the elastic energy is consumed, thus attaining the final regime in Fig. 2*C*.

Modeling. The expansion of the rupture opening produces a strain in the membrane defined by a strain tensor, $\boldsymbol{\varepsilon}$, which is discussed in greater detail in *SI Appendix*. The hoop deformation of the rim ($\varepsilon_{\theta\theta}$) up to the inception of cracking (Fig. 2*D*) is used to estimate the hoop surface stress as $\sigma_{\theta\theta} = E_s^{'}\varepsilon_{\theta\theta}$, with $E_s^{'}$ as the surface dilatational elastic modulus (*SI Appendix*), shown in Fig. 2*E*. The result does not change if one considers the expected change in the surface elastic modulus due to the change in BSA concentration during the rim retraction. For larger surface concentrations (20, 35, and 50 mg/mL), stress data are reported up to the appearance of cracks since, when cracks develop, the actual stress cannot be easily estimated. It is apparent that at larger BSA concentrations, the stress level attained at the onset of cracks does not depend on BSA concentration, $\sigma_{\theta\theta}^{b}$ in Fig. 2*E*, while for $c_{\mathrm{BSA}} < 20$ mg/mL, that is, when cracks do not form, such a critical stress is not attained. In passing, it is worth remarking that the critical hoop surface stress is comparable with the surface elastic dilatational modulus in agreement with results of Tabuteau et al. (22) for brittle fractures in viscoelastic fluids. We identify the conditions for the bubble flowering in the value of E_c; when it is bigger than one, the initial dilatational modulus is sufficiently high to induce fragile cracks on the opening rim,

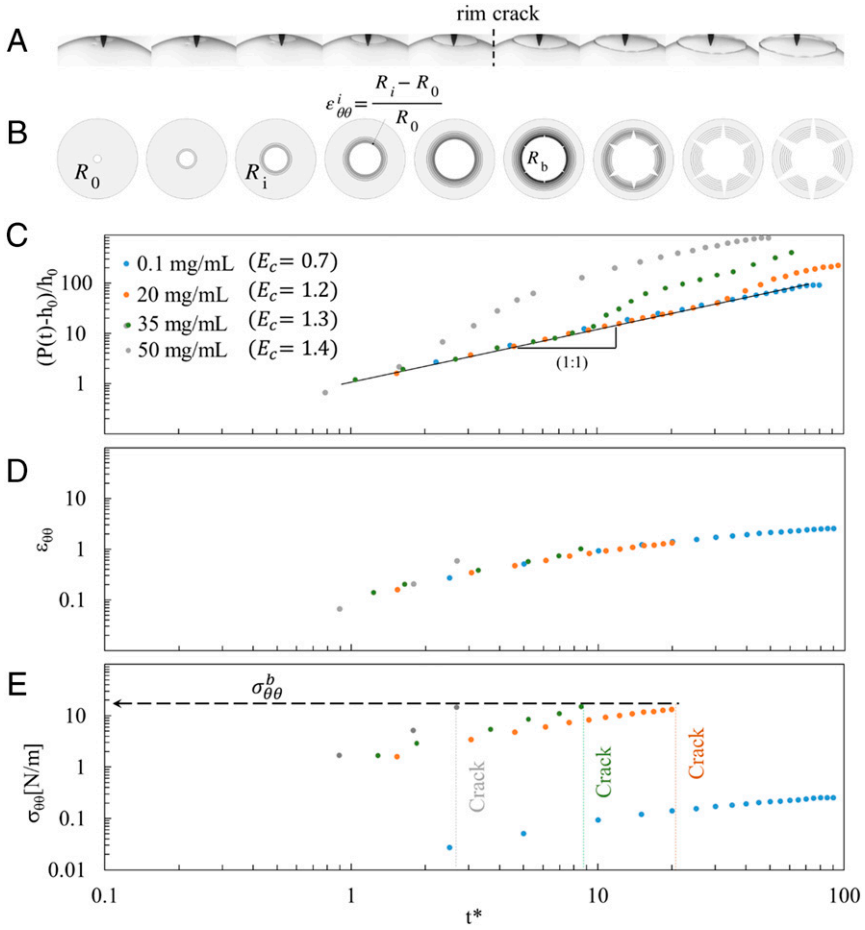

Fig. 2. Two-step mechanism to form bubble flowering. (*A*) Experimental evidences of two rupture regimes for BSA concentration equal to 20 mg/mL. (*B*) Rim deformation ($\varepsilon^i_{\theta\theta}$) sketched in the two rupture regimes, where R_i is the rim radius at time i and R_0 is the initial rim radius. (*C*) Dimensionless perimeter as function of dimensionless time $\left(t^* = \frac{t}{\frac{\mu R}{\gamma}}\right)$, where t is the experimental time and P_0 is the perimeter of the first observed hole. (*D*) Hoop strain as function of dimensionless time, calculated as shown in *SI Appendix*. (*E*) Hoop surface stress ($\sigma_{\theta\theta}$) as function of dimensionless time is calculated as $\sigma_{\theta\theta} = E_s^{'}\varepsilon_{\theta\theta}$.

while when it is less than one, the surface tension drives the bursting phenomenon.

Analyzing the crack formation and the successive bubble flowering, it is useful to compare the observations presented here with what has been established for filaments of viscoelastic liquids that break with brittle cracks in uniaxial extensional flows at sufficiently high Weissenberg numbers, defined as $Wi = \dot{\varepsilon}_{\theta\theta}\lambda$, where $\dot{\varepsilon}_{\theta\theta}$ is the hoop strain rate and λ is the surface relaxation time as calculated in *SI Appendix* (21). The number of cracks is also found to be proportional to the diameter of the filament at the crack formation (23). The present experiments represent biaxial stretching of viscoelastic films and complement the stretching of viscoelastic filaments but with important distinctions. In the experiments reported here, the hole opening the rim is subjected to an extensional flow that is modeled as a uniaxial stretching with strain rate given by $\dot{\varepsilon}_{\theta\theta}$ measured at the rim border ($\dot{\varepsilon}_{\theta\theta} = \frac{u}{R}$), and the formation of multiple cracks determines the number of observed petals in the flowering. We here propose a simple argument to predict the number of petals in bubble flowering based on three assumptions: 1) all the fluid of the disappearing film collects into the rim, and 2) film drainage is negligible (24, 25), and 3) the BSA accumulates on the rim from the disappeared film. The actual volume of the rim is $V_R = 2\pi^2 r^2 R$, with $R(t)$ the actual major radius and $r(t)$ the minor radius of the toroidal uncracked rim (Fig. 3*A*), which here plays the role of the filament. The volume of the material subtracted from the bubble by the advancing rim is $V_S = \pi R^2 h$. Mass conservation implies $V_R = V_S$, and, assuming no drainage during the bubble inflation (as verified by interferometric measurements in *SI Appendix*) and that the assumption that the number of cracks is proportional to the filament diameter (23), the number of petals scales as $R_b^{\frac{1}{5}}$ (Fig. 3*B*). The experimental results, in terms of hole radius at crack inception and the number of observed cracks, support this scaling as shown in Fig. 3*A*. Furthermore, the experiments show that the rim breaks when the local BSA concentration in the rim reaches the same value (of that corresponding to the critical stress defined above). Hence, data from one experiment can be used to determine this critical concentration, C^*_{rim}, and for calculating the number of petals formed during bubble flowering (Fig. 3*A*) in subsequent experiments. The critical concentration is well defined by the propagation of independent, simultaneous, multiple cracks that resemble a brittle fracture. Usually, in solids, a brittle fracture starts from microimperfections in the material; in our viscoelastic thin rim, the brittle fracture, which arises due to the high E_c and deformation rate, may also start from microimperfections, which are not able to heal sufficiently fast. Qualitatively, we can speculate that the

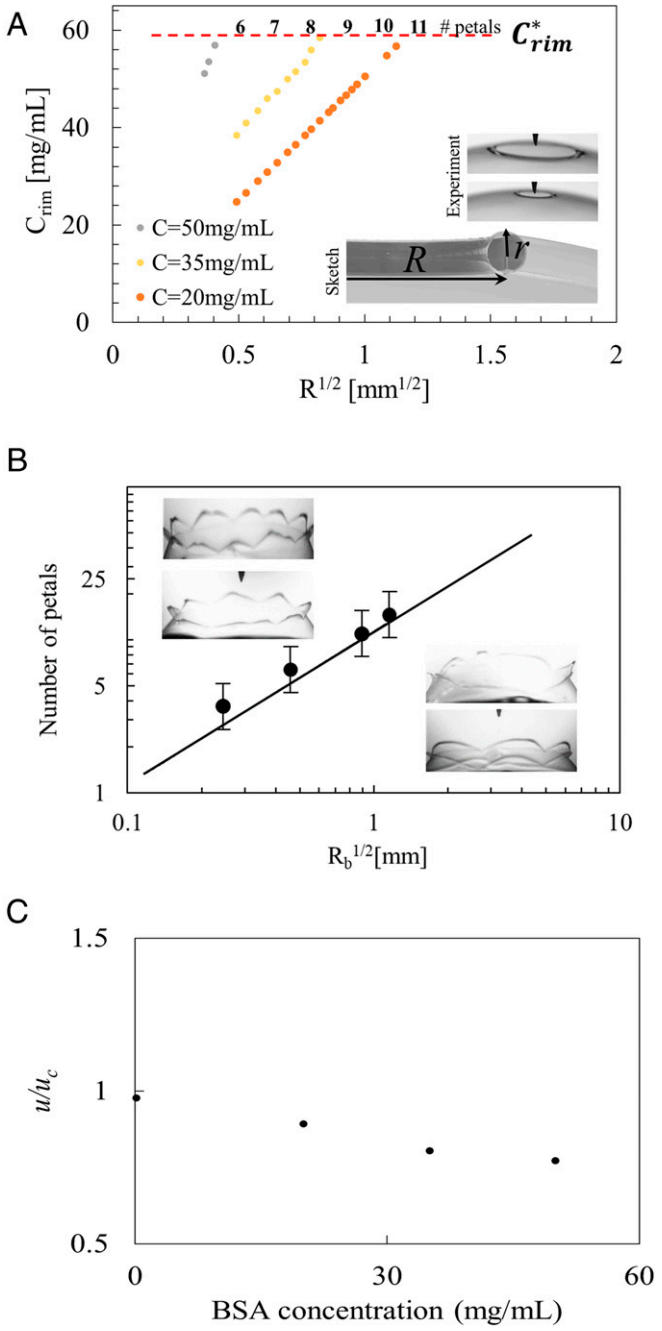

Fig. 3. Characterization and modeling of bubble flowering formation. (*A*) The concentration of BSA in the rim, C_{rim}, is plotted as function of the root mean square of the hole radius *R*. It is calculated as $C_{rim} = C\frac{S_s}{S_r}$, where *C* is the BSA concentration, S_s is the surface of the opening disk ($S_s = 2\pi R^2$), and S_r is the surface of the toroidal rim ($S_r = 4\pi^2 r R$). (*Inset*) Magnification on the toroidal rim observed experimentally and the schematic view for the definition of the geometrical parameters defined in the text. (*B*) From *A*, the number of petals is plotted versus the square root of *R* at crack. (*C*) Rim velocity, *u*, at different concentrations of BSA.

number of possible imperfections depends on how much surface is created by the rim opening, and so, on R_b.

To confirm the hypothesis of the effect of the surface viscoelasticity, we added an additional surfactant (i.e., Polysorbate 80 (Tween 80) as described in *SI Appendix*) that competes for surface coverage with BSA. The reduced elasticity on the surface because of the entrance of the new surfactant suppressed the flowering, and the bubble bursting returns to the inertial regime (Fig. 4). These results were confirmed also with a different surface-active polymer, that is, polyethylene glycol (PEG). PEG is known to be surface active and can form a monolayer at an air/water interface as well as a self-assembled film from an aqueous solution (26–30). Experiments of bubble bursting were performed using solutions of PEG and BSA + PEG. The experimental observations show that when a small amount of PEG (1 or 2 mg/mL) is added to a BSA solution (i.e., 50 mg/mL), the bubble flowering is suppressed, and the bursting dynamics are very similar to the ones without BSA. The interfacial rheology of the tested systems is detailed in *SI Appendix*.

Conclusion

In summary, we show that under certain conditions, the bursting of bubbles with viscoelastic interfaces displays a flowering-like morphology. It is possible to control the bubble flowering phenomenon by adjusting the surface viscoelasticity by varying the protein concentration and suppressing bubble flowering with the use of surfactants. These results are relevant to processes in which the fragmentation of interfaces as a result of bubble bursting is important:

a) In nature, a known example is the stress-induced fragmentation by intense hydrodynamic flows that is used by marine organisms such as macrophyte algae and coral colony for vegetative reproduction. Recently, on a microscopic scale, the hydrodynamic forces in bursting bubbles were addressed to be the reason of DNA nanotube fragmentation (6).
b) In industrial bioengineering, a well-known example is cell culture in bioreactors in which the cells are grown in a nutrient medium having usually viscoelastic interfaces. For the production of a vaccine, the cell cultures are then infected with viruses, which reproduce and serve as the basis of a vaccine. In this frame, the production can suffer cell death and fragmentation caused by the bubble bursting at the liquid surface (7).

Our findings present insight for understanding and optimization of all these processes.

Materials and Methods

A simple experimental device is used to form bubbles from a bulk liquid. A cylinder made of Teflon with a radius of ca.7.5 mm is pulled out from a liquid pool to produce a flat liquid film that is inflated with air at a constant flow rate by a syringe pump. The growing bubble is punctured when it reaches a radius of curvature equal to the cylinder radius by a metal needle, and the bursting is recorded by using a high-speed camera (additional details on the methods are given in *SI Appendix*). BSA solutions were made by dissolving measured masses of the lyophilized powder with phosphate-buffered solution (as it is discussed in greater detail in *SI Appendix*).

Data Availability. All study data are included in the article and/or supporting information.

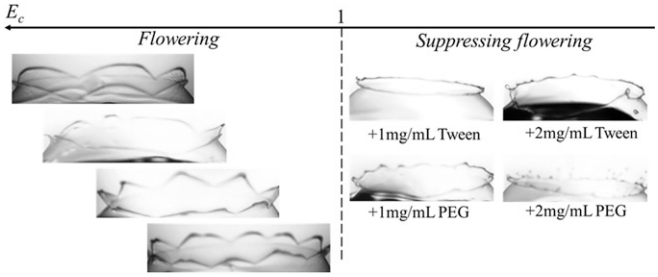

Fig. 4. Bubble flowering at different E_c. The flowering is suppressed when E_c is minor than 1.

1. H. Lhuissier, H. Villermaux, Bursting bubble aerosols. *J. Fluid Mech.* **696**, 5–44 (2012).
2. L. Champougny, M. Roché, W. Drenckhan, E. Rio, Life and death of not so "bare" bubbles. *Soft Matter* **12**, 5276–5284 (2016).
3. J. C. Bird, R. de Ruiter, L. Courbin, H. A. Stone, Daughter bubble cascades produced by folding of ruptured thin films. *Nature* **465**, 759–762 (2010).
4. D. Tammaro *et al*., Elasticity in bubble rupture. *Langmuir* **34**, 5646–5654 (2018).
5. D. Tammaro *et al*., Validated modeling of bubble growth, impingement and retraction to predict cell-opening in thermoplastic foaming. *Chem. Eng. J.* **287**, 492–502 (2016).
6. R. F. Hariadi, E. Winfree, B. Yurke, Determining hydrodynamic forces in bursting bubbles using DNA nanotube mechanics. *Proc. Natl. Acad. Sci. U.S.A.* **112**, E6086–E6095 (2015).
7. G. D. Robson, J. Puci, W. Throndset, N. Dunn-Coleman, Oxidative stress, fragmentation and cell death during bioreactor growth of filamentous fungi. *British Mycological Society Symposia Series* **27**, 129–142 (2008).
8. G. Debrgeas, P. de Gennes, F. Brochard-Wyart, The life and death of "bare" viscous bubbles. *Science* **279**, 1704–1707 (1998).
9. F. E. C. Culick, Comments on a ruptured soap film. *J. Appl. Phys.* **31**, 1128–1129 (1960).
10. W. R. McEntee, K. J. Mysels, Bursting of soap films. I. An experimental study. *J Phys. Chem.* **73**, 3018–3038 (1969).
11. P. L. L. Walls, L. Henaux, J. C. Bird, Jet drops from bursting bubbles: How gravity and viscosity couple to inhibit droplet production. *Phys. Rev. E Stat. Nonlin. Soft Matter Phys.* **92**, 021002 (2015).
12. M. S. Bhamla, C. E. Giacomin, C. Balemans, G. G. Fuller, Influence of interfacial rheology on drainage from curved surfaces. *Soft Matter* **10**, 6917–6925 (2014).
13. L. G. Cascão Pereira, O. Théodoly, H. W. Blanch, C. J. Radke, Dilatational rheology of BSA conformers at the air/water interface. *Langmuir* **19**, 2349–2356 (2003).
14. M. Campana *et al*., Adsorption of bovine serum albumin (BSA) at the oil/water interface: A neutron reflection study. *Langmuir* **31**, 5614–5622 (2015).
15. A. Jaishankar, V. Sharma, G. H. McKinley, Interfacial viscoelasticity, yielding and creep ringing of globular protein–surfactant mixtures. *Soft Matter* **7**, 7623–7634 (2011).
16. X. Chen *et al*., Specific anion effects on water structure adjacent to protein monolayers. *Langmuir* **26**, 16447–16454 (2010).
17. D. O. Grigoriev, S. Derkatch, J. Krägel, R. Miller, Relationship between structure and rheological properties of mixed BSA/Tween 80 adsorption layers at the air/water interface. *Food Hydrocoll.* **21**, 823–830 (2007).
18. A. Kannan, I. C. Shieh, D. L. Leiske, G. G. Fuller, Monoclonal antibody interfaces: dilatation mechanics and bubble coalescence. *Langmuir* **34**, 630–638 (2018).
19. G. H. McKinley, *Visco-Elasto-Capillary Thinning and Break-Up of Complex Fluids* (Annual Rheology Reviews, 2005).
20. P. C. Petit, M. Le Merrer, A.-L. Biance, Holes and cracks in rigid foam films. *J. Fluid Mech.* **774**, R3 (2015).
21. Q. Huang, O. Hassager, Polymer liquids fracture like solids. *Soft Matter* **13**, 3470–3474 (2017).
22. H. Tabuteau, S. Mora, M. Ciccotti, C. Y. Hui, C. Ligoure, Propagation of a brittle fracture in a viscoelastic fluid. *Soft Matter* **7**, 9474–9483 (2011).
23. Q. Huang, N. J. Alvarez, A. Shabbir, O. Hassager, Multiple cracks propagate simultaneously in polymer liquids in tension. *Phys. Rev. Lett.* **117**, 087801 (2016).
24. S. Vandebril, A. Franck, G. G. Fuller, P. Moldenaers, J. Vermant, A double wall-ring geometry for interfacial shear rheometry. *Rheol. Acta* **49**, 131–144 (2010).
25. J. M. Frostad, D. Tammaro, L. Santollani, S. Bochner de Araujo, G. G. Fuller, Dynamic fluid-film interferometry as a predictor of bulk foam properties. *Soft Matter* **12**, 9266–9279 (2016).
26. Z. A. Zell, L. Isa, P. Ilg, L. G. Leal, T. M. Squires, Adsorption energies of poly(ethylene oxide)-based surfactants and nanoparticles on an air-water surface. *Langmuir* **30**, 110–119 (2014).
27. B. A. Noskov, A. V. Akentiev, G. Loglio, R. Miller, Dynamic surface properties of solutions of poly (ethylene oxide) and polyethylene glycols. *J. Phys. Chem. B* **104**, 7923–7931 (2000).
28. A. Kannan, I. C. Shieh, G. G. Fuller, Linking aggregation and interfacial properties in monoclonal antibody-surfactant formulations. *J. Colloid Interface Sci.* **550**, 128–138 (2019).
29. L. Lombardi, D. Tammaro, Effect of polymer swell in extrusion foaming of low-density polyethylene. *Phys. Fluids* **33**, 033104 (2021).
30. V. Chandran Suja, M. Rodríguez-Hakim, J. Tajuelo, G. G. Fuller, Single bubble and drop techniques for characterizing foams and emulsions. *Adv. Colloid Interface Sci.* **286**, 102295 (2020).